ACS Catalysis

Research Article

pubs.acs.org/acscatalysis

Morphological Effects of Gold Clusters on the Reactivity of Ceria Surface Oxygen

Jin Wang, Hongyi Tan, Shuzhen Yu, and Kebin Zhou*

School of Chemistry and Chemical Engineering, University of Chinese Academy of Sciences, Beijing 100049, P.R. China

S Supporting Information

ABSTRACT: Well-defined {100}-faceted ceria nanocube-supported gold nanoclusters with various morphologies, including individual atom, monolayer, multilayer and nanoparticle, have been synthesized and systematically investigated combined with density functional theory calculations. A strong morphological effect of gold clusters on the reactivity of ceria surface oxygen has been identified. The reducibility and CO oxidation activities of Au/CeO_2 catalysts increased significantly as the morphology of the gold clusters changed from single atoms to monolayer, then to multilayer, then nanoparticles. It was revealed that up to a bilayer of gold clusters were needed for desirable catalytic performance in the Au/CeO_2 system. The transfer of electrons from gold clusters to the surface Ce−O groups of ceria and strong Au−Au interactions play significant roles in determining the reducibility of surface oxygen of CeO_2.

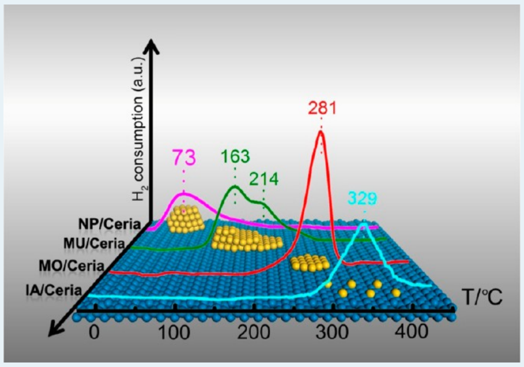

KEYWORDS: *gold, morphological effect, ceria, nanocatalysis, surface oxygen*

1. INTRODUCTION

Gold nanoparticles (NPs) supported on metal oxides exhibit exceptional catalytic properties for many reactions, such as low-temperature CO oxidation,[1] hydrogenation,[2] and selective oxidation.[3] Although numerous studies have been carried out to elucidate the origin of the unique properties of gold NPs, the nature of active Au species and their structures are still widely debated even for CO oxidation.[4] It is generally accepted that the size of gold NPs is of paramount importance,[5] and up to eight atoms are necessary for CO oxidation.[6] In 2004, Goodman et al.[7,8] found that TiO_2-supported Au clusters at approximately 3.5 nm exhibited maximum reactivity at diameters between 1 to 6 nm. They ascribed the pronounced size-dependent activity of the supported Au clusters to the distinctive band gap of two-atom-thick clusters, which describes a quantum size effect of gold bilayer structures. In 2008, Hutchings and colleagues[9] reported that the subnanometer gold clusters with ~10 atoms on a FeO_x support, rather than other species such as individual Au atoms, monolayer structures, and gold NPs, were directly responsible for the catalytic activity. It was found that the Au_{10} cluster also exhibited bilayer morphology. These studies indicate that the morphology of gold may be crucial to the reactivity of subnanometer gold species. So far, however, there have been no systematic studies reported on the morphological effects of gold clusters except for a few theoretical calculations.[10−12]

The support also plays a key role in the performance of gold catalysts.[6,13,14] Among various metal oxides, ceria (CeO_2) has proven to be useful in a wide variety of catalytic applications because of its superior Ce^{4+}/Ce^{3+} redox couple and oxygen storage capacity.[15] Once gold has been deposited on the ceria surface, gold−ceria interfaces can be formed. The −Au−O−Ce− species in the perimeter of the interface were considered as active sites for several reactions.[16−19] The oxygen vacancies at the interfaces could absorb and activate O_2,[20,21] and the interfacial microstructure even determined whether ceria-supported gold catalysts were active or not for CO oxidation.[22]

Herein, in combination with density functional theory (DFT) calculations, we report a systematically comparative study of {100}-faceted CeO_2 nanocube(NC)-supported gold clusters with four different morphologies, individual atom (IA), monolayer (MO), multilayer (MU), and nanoparticle (NP). Well-defined faceted ceria was employed to build a model surface to clarify the interfacial structure.[23,24] Interestingly, as the morphology of gold clusters changed from single atom to monolayer, multilayer, then nanoparticle, the reducibility of Au/CeO_2 catalysts increased remarkably. It was found that gold species up to the bilayer was necessary for desirable catalytic performance in Au/CeO_2 systems.

2. EXPERIMENTAL SECTION

2.1. Preparation of Catalysts. All materials used in this study were analytical purity.

Preparation of CeO_2 NCs. CeO_2 nanocubes were synthesized by using a facile hydrothermal method. One gram of $Ce(NO_3)_3{\cdot}6H_2O$ was dissolved in deionized water (10 mL), then an aqueous NaOH solution (2.5 M, 40 mL) was added rapidly with continuous stirring at room temperature for 5 min.

Received: December 21, 2014
Revised: March 24, 2015
Published: March 26, 2015

DOI: 10.1021/cs502055r
ACS Catal. 2015, 5, 2873−2881

The mixture was transferred to a 50 mL Teflon-lined autoclave and heated at 190 °C for 20 h. After the reaction ran to completion, the products were washed with deionized water and alcohol several times, then dried at 50 °C for 2 h, and calcined in air at 350 °C for 3 h.

Preparation of the Colloidal Au Nanoparticles (2–5 nm). In a typical procedure, 0.03 g of PVA, which was used as protecting agent, was added to an aqueous $HAuCl_4$ solution (0.11 mM, 450 mL) under vigorous stirring. After 5 min under stirring, an aqueous solution of $NaBH_4$ (0.02 M, 4 mL) was added to the above solution rapidly. The color of the mixture changed from canary yellow to orange-brown, indicating the gold sol was obtained.

Preparation of CeO_2 NCs-Supported Gold Nanoparticles Catalyst (NP/Ceria):[19] An appropriate amount of CeO_2 NCs powder was dispersed in deionized water and sonicated for 10 min. The obtained slurry was added to the above gold sol rapidly with continuous stirring for 2 h before the discoloration of the upper layer of the solution. Then, the obtained precipitate was washed with deionized water and ethanol and dried at 50 °C for 5 h, followed by activating at 300 °C for 1 h under reactant gases containing 1.0 vol % CO in air. Catalysts with theoretically calculated gold loadings of 0.45 and 1.50 wt % were prepared and denoted as NP/ceria-1 and NP/ceria-2, respectively.

Preparation of CeO_2 NCs-Supported Gold Individual Atom Catalyst (IA/Ceria):[25] The methyl halide (CH_3I) treatment method was adopted to obtain the IA/ceria samples. Typically, 0.5 g of an NP/ceria-1 sample is placed in a quartz tubular reactor and calcined under pure N_2 with a flow rate of 60 $mL\cdot min^{-1}$ at 150 °C for 30 min, followed by CH_3I treatment by changing the gas from pure N_2 to CH_3I/N_2 (saturator at 50 °C). Then, the product was treated with a hot aqueous NaOH solution (0.1 M) to remove any halide species, then washed and dried at 50 °C for 5 h, followed by activating at 300 °C for 1 h under reactant gases containing 1.0 vol % CO in air.

Preparation of CeO_2 NCs-Supported Monolayer Gold Catalyst (MO/Ceria). The MO/ceria catalyst was prepared following the CH_3I treatment process for IA/ceria (*vide supra*). The only variation was that NP/ceria-2 was used as the starting material.

Preparation of the CeO_2NCs-Supported Multilayer Gold Catalyst (MU/Ceria). The MU/ceria catalyst was obtained by redox-treating of the MO/ceria sample. Typically, an appropriate amount of MO/ceria is reduced in a fixed-bed quartz tubular reactor under a flow of 60 $mL\cdot min^{-1}$ in H_2 (5 vol % hydrogen, balance argon) at 600 °C for 30 min. Subsequently, the gas mixture (20.8% oxygen, balance nitrogen) is passed through the reactor for 30 min at 600 °C, followed by activating at 300 °C for 1 h under reactant gases containing 1.0 vol % CO in air.

2.2. Catalyst Characterizations. The size and morphology images of all samples were obtained with a JEOL JEM-1200EX transmission electron microscope (TEM) and a FEI Tecnai F20 high-resolution transmission electron microscope (HRTEM). The Au loading was measured with a Varian Vista MPX Inductively Coupled Plasma Optical Emission Spectrometer (ICP-OES). The X-ray diffraction (XRD) measurements for structure determination were carried out with a Bruker D8 Advance X-ray diffractometer with Cu Kα radiation ($\lambda = 1.5418$ Å), and the data were recorded at a scan rate of 4 $degree\cdot min^{-1}$. Au_{4f} and Ce_{3d} photoelectron spectra were taken using X-ray photoelectron spectroscopy (XPS, ESCALAB 250 Xi) with Al Kα radiation. HAADF-STEM images and energy dispersive X-ray spectrometry (EDS) analysis were acquired with a Titan G2 80–200 with the probe Cs-corrector configuration at 200 kV. The X-ray absorption spectra were measured at the 1W2B beamline with a Si (111) double-crystal monochromator in the Beijing Synchrotron Radiation Facility (BSRF), China. Au L_{III}-edge absorption spectra were obtained in a transmission mode at room temperature. The typical electron beam energy and the current were 2.5 GeV and 200 mA, respectively. EXAFS data were analyzed using the IFEFFIT data analysis package to correct the background signal and to normalize the intensity. Hydrogen temperature-programmed reduction (H_2-TPR) analysis was carried out with a ChemiSorb 2720 apparatus equipped with a TCD detector by heating the catalysts at 10 $deg\cdot min^{-1}$ to 700 °C, in a 5 vol % H_2/Ar mixture flowing at 25 $mL\cdot min^{-1}$. All the characterizations were carried out after treatment under a CO/O_2 mixture (activity reactant gas atmosphere) at 300 °C for 1 h.

2.3. Catalyst Activity Evaluation. The CO oxidation activities of the catalysts for were evaluated at atmospheric pressure in a continuous flow fixed-bed quartz tubular reactor. The catalyst powder (0.10 g) was placed in the reactor. The reactant gases (1.0 vol % CO in air) flowed through the reactor at a rate of 50 $mL\cdot min^{-1}$. Each catalyst was filled in the middle of the quartz tubular reactor and was heated in a ceramic furnace. The composition of the gas exiting the reactor was monitored by gas chromatography.

2.4. Theoretical Calculations. We used the basis of the plane-wave DFT+U approach with a value of $U = 5$ eV, and all calculations were performed by using the Vienna *ab initio* simulation package (VASP), as we previously reported.[19] The ionic cores and electron–ion interactions were described by the projector augmented wave (PAW) method with a cutoff energy of 500 eV to limit the plane-wave basis set, and the electron exchange and correlation energies were calculated with the GGA-PW91 functional. For all calculations in this present study, spin-polarization was performed. A reconstructed CeO_2 (100) surface model was used in which half of the top oxygen atoms were moved to the bottom.[26] The 3 × 3 supercell surface model with 7 atomic layers was employed, in which the three bottom layers were fixed and a vacuum region of 20 Å was inserted between periodic images. Otherwise, other parameters including Monkhorst–Pack k-point meshes of 2 × 2 × 1, the difference in total energy between two consecutive ionic steps of less than 10^{-4} eV and the allowed maximum force of 0.02 $eV\cdot Å^{-1}$ were unchanged from the previous report. To describe the interactions between the CeO_2 (100) surface and the Au species, we defined two energies: the adsorption energy (E_{ad}) and the vacancy formation energy (E_{vac}):

$$E_{ad} = E_T(Au_n/CeO_2) - E_T(CeO_2) - E_T(Au_n)$$

$$E_{vac} = E_T(Au_n/CeO_{2-x}) + 1/2E_T(O_2) - E_T(Au_n/CeO_2)$$

where E_T (Au_n/CeO_2) and E_T (Au_n/CeO_{2-x}) are the energies of Au_n adsorbed on stoichiometric CeO_2 and reduced CeO_2 with a single O vacancy, respectively, and E_T (CeO_2), E_T (Au_n), and E_T (O_2) are the energies of the clean slab, the Au clusters and the O_2 molecule, respectively. Here, n represents the number of Au atoms in the Au cluster.

3. RESULTS AND DISCUSSION

CeO_2 NCs-supported gold NPs catalysts (NP/ceria) were prepared by the colloidal deposition method. Figure 1a and Figure S1−S2 show the TEM and HRTEM images of NP/ceria catalysts with Au loadings of 0.45 and 1.50 wt % labeled as NP/ceria-1 and NP/ceria-2, respectively. It can be observed that gold NPs (2−5 nm) are homogeneously dispersed on the surfaces of CeO_2 NCs, resulting in well-defined metal/support interfaces. Following the strategy developed by Hardacre et al.,[27] methyl halide (CH_3I) treatment of NP/ceria was employed to obtain highly dispersed gold species. Figure 1b and Figure S3 show the sample of iodide-treated NP/ceria-1 (denoted as IA/ceria). After iodide treatment, gold NPs could not be observed on the surface of the ceria support. Similar results were obtained from the iodide-treated NP/ceria-2 sample (denoted as MO/ceria), as shown in Figure 1c and Figure S4. Even after further high temperature (600 °C) redox treatment, Au NPs were still absent, as shown in Figure 1d and Figure S5 (denoted as MU/ceria). ICP-OES measurements demonstrated that all of the initial Au content remained unchanged after treatment. This indicates that the initial Au nanoparticles may completely disperse into smaller Au species after iodide- or further redox-treatment. Similar results had been reported in Au/C,[27] and Au/TiO_2 systems.[28] In addition, X-ray powder diffraction patterns (XRD) show that Bragg reflections of gold were not observed among the Au/CeO_2 catalysts except for NP/ceria-2 (Figure S6) because of the small size of the gold species. X-ray fluorescence spectrum analysis (XRF) and X-ray photoelectron spectroscopy (XPS) measurements were made, and it turned out that iodine could not be detected (Figure S7).

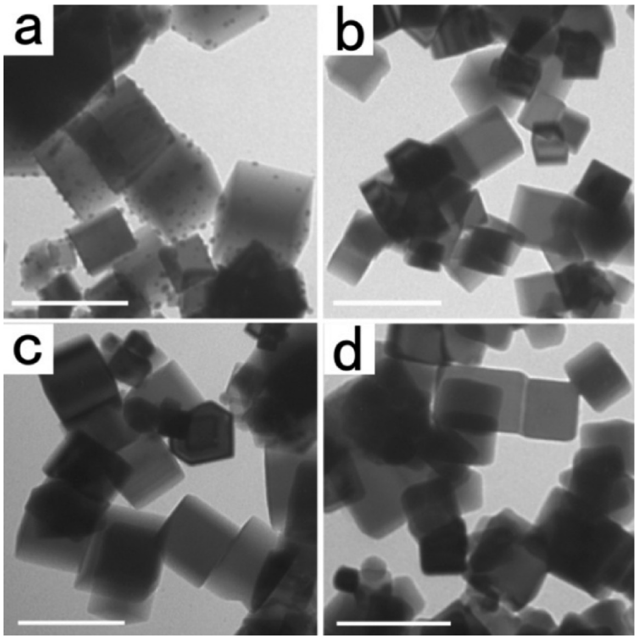

Figure 1. TEM images of Au/CeO_2 catalysts: (a) NP/ceria-2, (b) IA/ceria, (c) MO/ceria, (d) MU/ceria. Scale bar is 100 nm.

High-angle annular dark field scanning transmission electron microscopy (HAADF-STEM) has become an effective technique for analyzing structures at the atomic level because it provides directly interpretable images.[29] The implementation of spherical aberration correction (C_s) in HAADF-STEM and quantitative analysis of HAADF-STEM images using statistical parameter estimation theory enable this technique to achieve single-atom sensitivity[30] and 3D reconstructions of NPs.[31,32] Thus, the four Au/CeO_2 catalysts were characterized by aberration-corrected STEM in HAADF modes, and the representative HAADF-STEM images are shown in Figure 2. The atomic morphologies of gold species were obtained by employing a quantitative image analysis method that involves fitting the overlapping atom intensities to two-dimensional Gaussian functions and statistical theory.[30,33]

It shows that the arrangement of Ce atoms in all of the catalysts is uniform. Compared with pure ceria (Figure S8), it can be found that some distinct bright spots are distributed on the surface and exactly occupy the top position of Ce atoms from Figure 2A$_1$ and Figure S9a for the IA/ceria sample. These spots can be assigned to single Au atoms. However, surface Au species, especially individual Au atoms, were not as clearly distinguished from the CeO_2 substrate as from Au/MgO, Pt/FeO_x and Au/C[34−36] because the difference in Z between the Au and Ce atoms is only 21. Because the incoherently scattered intensity I_{HAADF} of HAADF-STEM is simply the sum of the contributions of each atom, $I_{\mathrm{HAADF}} = \kappa NZ^{\alpha}$, where κ is a constant, N is the number of atoms with a given volume V and Z is atomic number. The exponent α is close to 2 based on the Rutherford scattering value.[37] Therefore, the quality of images depends on not only the condition of the experiment but also the difference in atomic number (Z) between elements in the sample, especially the latter. Fortunately, quantitative analyses of images enable us to achieve single-atom sensitivity.[31,38] According to quantitative analysis (Figure A$_2$−A$_4$ and S9), only two intensities of the atomic column were detected across the whole picture; they were ascribed to top-Ce and Au adatoms, respectively. In the top-view image of the two-dimensional Gaussian-function fitting intensity of per atoms (Figure 2A$_2$), it can be observed that several individual Au atoms (red spot) are dispersed on the surface of ceria. For the sample of MO/ceria (Figure 2B and Figure S10), there are many single Au atoms spread over the surface and still adsorbed on the top sites of Ce. Compared with IA/ceria, the only difference is that the distance between Au adatoms is shorter. Thus, the Au species in this catalyst is defined as a monolayer structure. The HAADF-STEM images of MU/ceria (Figure 2C, Figure S11) show clear variations in atomic column intensity, revealing that several types of gold species are present on the surface of CeO_2. A detailed quantitative analysis procedure of the data is shown in Figure S12. Through fitting the overlapping atom intensities to two-dimensional Gaussian functions, a two-dimensional Gaussian-function fitting model was obtained. The three-dimension curved surface was plotted to describe the pixel values of the HAADF-STEM image fitting model (Figure 2C$_2$ and 2C$_3$). The intensity value increased as the color changed from blue to red. The good agreement with experiment contrast proves the good quality of this method (Figure S12e). According to the histogram of intensities (Figure S12f), there are four main peaks, and the mean intensity values increase linearly as a function of the number of Au atoms. Because the total integrated HAADF intensity of columns in a scaled cluster is proportional to the number of gold atoms,[31,39] the four intensity values in Figure 2C$_4$ define them from low to high as standard values for Ce atom, monolayer, bilayer and three-layer Au structures, respectively. Moreover, analysis of other regions also gave the same results (Figure S13). Therefore, three types of Au morphologies coexist in samples of MU/ceria, which

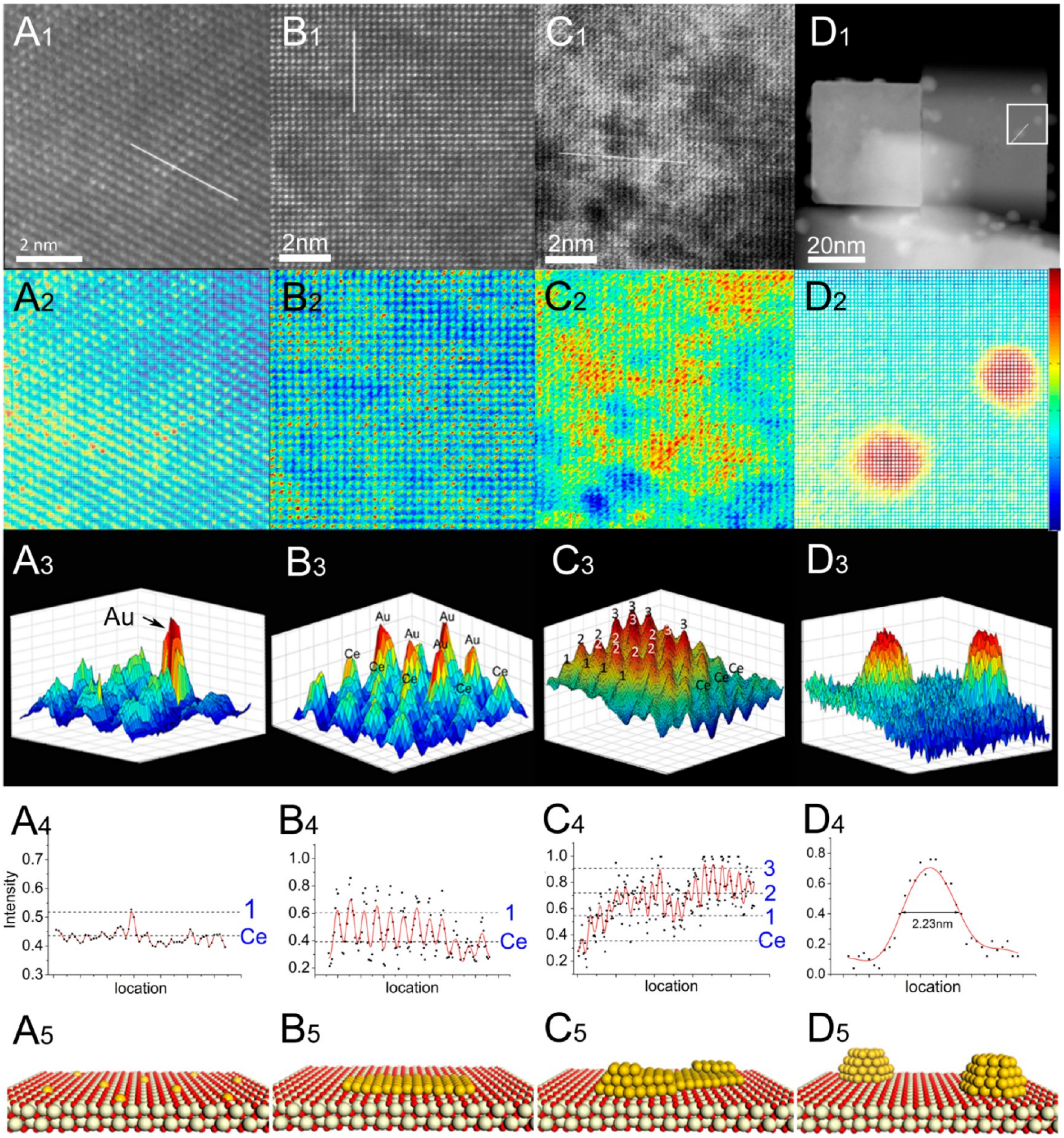

Figure 2. HAADF-STEM images and analysis of four catalysts: (A) IA/ceria, (B) MO/ceria, (C) MU/ceria, (D) NP/ceria-2. (1) Experimental images; (2) Top view of two-dimensional Gaussian-function fitting intensity profiles of per atom (A_2, B_2, C_2) and cluster density profile (D_2), intensity value increasing from blue to red. (3) Side view of magnification in A_2, B_2, C_2 and D_2. (4) Atom intensity profiles along white line in A_1, B_1, C_1 and cluster intensity profile along white line in D_1; numerals 1, 2, and 3 indicate the numbers of the Au atomic layer; (5) Corresponding structural models.

correspond well with the three reduction peaks from the TPR results. Based on STEM images (Figure $2D_1$ and Figure S14), intensity mapping (Figure $2D_2$ and $2D_3$), and EDS mapping (Figure S15) of NP/ceria, gold NPs are dispersed and strongly anchored onto the surface of ceria, which can be observed clearly without any image analysis. On the basis of characterizations and analysis described above, {100}-faceted CeO_2 NCs-supported gold clusters with four different morphologies (i.e., IA, MO, MU and NP) have been resolved, and models of Au/CeO_2 catalysts were constructed to reflect the morphology differences of gold species among them and are shown in Figure $2A_5$−D_5.

X-ray absorption measurements of gold nanoclusters on ceria were carried out at the Au L_{III} edge (nearly 11919 eV). The X-ray absorption near edge structure (XANES) spectra of all the Au/ceria catalysts and the reference compounds, including Au foil and Au_2O_3, are shown in Figure 3A and Figure S16, respectively. Only a shoulder at approximately 11 930 eV is observed for the Au foil at the Au L_{III} edge, whereas Au (III) exhibits a large threshold absorption peak at the edge (white line, 11 927 eV). According to the literature,[40] the absorption edge of Au (III) and Au (I) shifts to lower energy compared to the gold foil because of the low-energy dipole-allowed $2p_{3/2}$ to 5d transition that is allowed for $Au_2O_3(d^8)$ and forbidden for $Au^0(d^{10})$. In addition, the intensity of the white line is proportional to the density of unoccupied d states.[41] Therefore, the white line feature was usually used for the determination of the oxidation state of Au. As shown in Figure 3A, IA/ceria and MO/ceria exhibit absorption peaks at the L_{III} edge centered at energies of 11 927.5 and 11 930 eV, respectively, which are higher than that of the Au (III) L_{III} X-ray absorption edge. However, the intensities are much smaller than the intensity of Au (I).[42] Therefore, gold species of IA/ceria and MO/ceria are in the $Au^{\delta+}$ form. The absorption peak is missing from the spectra of MU/ceria and NP/ceria because of the complete occupancy of the d states,[43] indicating that the gold species are in the metallic state.

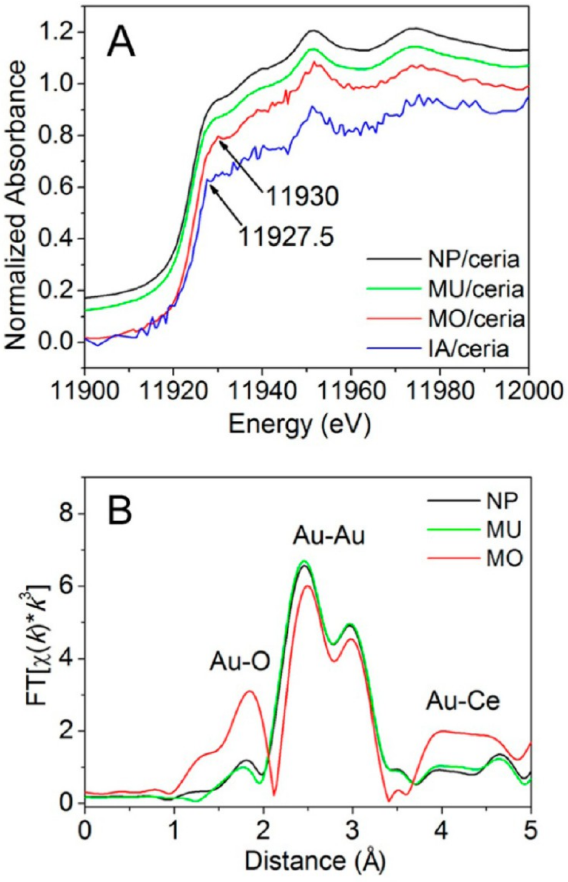

Figure 3. (A) XANES Au L_{III} of gold supported on ceria; (B) Fourier transform EXAFS functions of Au/ceria catalysts.

Extended X-ray absorption fine structure (EXAFS) of the Au/ceria samples was used to characterize the atomic structure of the Au species. Figure 3B shows the Fourier transformed EXAFS functions of the Au/ceria catalysts. The structural parameters (i.e., Au−Au coordination number (N) and interatomic distance (R_{Au-Au})) were obtained from the fitted first-shell Au L_{III} edge EXAFS spectra in the R space and are summarized in Table S1. For NP/ceria and MU/ceria, the Au−Au contribution is dominant as shown in the R-space. The interatomic distance (R) and the coordination number of 2.87 Å and ∼12 correspond to the first-shell spacing in the metallic gold clusters.[25] In the case of MO/ceria, remarkable Au−O and Au−Ce contributions appear in the spectra, indicating high dispersion of the gold species. The distance of Au−O is much larger than that in Au_2O_3, which should be attributed to interactions with the subjacent support.[34,44] The peak intensity of Au−O in the fitted data (Figure S17) is much lower than that in the experimental data because the Au−O contribution overlaps with the larger Au−Au contribution.[45] The coordination number around the central Au atoms decreases to 8, and a slight decrease of the Au−Au bond distance was found (from 2.87 to2.83 Å), due to the size evolution.[46,47] For samples of IA/ceria, it can be found that the height of the absorption edge is smaller than others (Figure 3A), which is caused by the low Au loading and the heavy Ce atoms. Due to the noise level, the contributions are too small to allow a confident assignment. Accurate determination of the Au−Au coordination number and the Au−O feature cannot be obtained from EXAFS. This result indicates a very high dispersion of Au on the support in the IA/ceria sample.

The valence states of gold species have a direct relationship with the behavior of Au-supported catalysts in some cases,[48] so XPS analysis was performed and the results are shown in Figure 4. It can be found that the peaks of Au $4f_{7/2}$ are present at 83.7 eV in samples of MU/ceria and NP/ceria-2, which are in agreement with the values for metallic Au.[17] In the case of IA/ceria and MO/ceria, the peaks of Au species shift approximately 0.2 eV toward high binding energy (BE). According to Karpenko et al.,[49] the upshift value (0.2 eV) here should be assigned to slightly positively charged gold ($Au^{\delta+}$), which agrees well with XANES analysis and may be caused by the change in chemical surroundings according to the HAADF-STEM results of these structures.

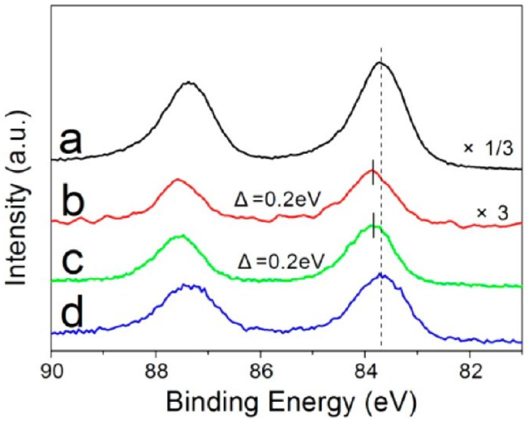

Figure 4. Au 4f photoelectron spectra profiles of Au/CeO_2 catalysts: (a) NP/ceria-2; (b) IA/ceria; (c) MO/ceria; (d) MU/ceria.

Temperature-programmed reduction (TPR) is a versatile technique to characterize the reducibility of a catalyst. It is well-known that TPR profiles of the Au/CeO_2 catalyst commonly exhibit three reduction peaks, located at low, mild, and high temperature regions, that can be assigned to interfacial Au−O−Ce species, surface and bulk oxygen of ceria, respectively.[50] Because the interfacial −Au−O−Ce− species are vital to their catalytic performances, we focused on the low-temperature regions here, and the results are shown in Figure 5. Similar to our previous study,[19] a reduction peak centered at approximately 73 °C appeared for NP/ceria. However, the reduction peak of the MO/ceria sample shifts up to 281 °C, showing that as the morphology of gold species changed from NPs to monolayer, the reducibility of the surface —Au—O—Ce— species decreases significantly. This situation becomes even worse in the case of IA/ceria catalyst, with the reduction peak at much higher temperature, 329 °C, indicating that —Au—O—Ce— species are hard to be reduced when individual gold atoms are deposited on the {100} surfaces of ceria. Interestingly, the reduction peak of MU/ceria appears in the temperature region between those for NP/ceria and MO/ceria. The peak is a superposition derived by three reduction components, namely, at 163, 214, and 281 °C, which can be assigned to the reduction of trilayer, bilayer, and monolayer gold-structure-related —Au—O—Ce— species, respectively. Based on the TPR results, it is clear that the morphology of gold species play a crucial role in determining the reducibility of the Au/CeO_2 catalyst: as the morphologies changed from single Au atom to monolayer, multilayer, then nanoparticle, the reducibility of Au/CeO_2 catalysts increases remarkably.

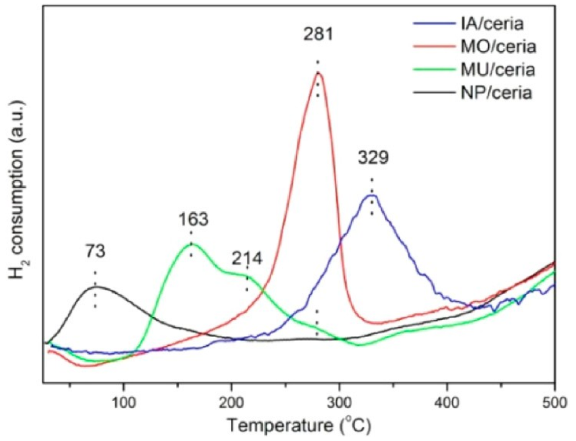

Figure 5. H_2-TPR profiles of Au/CeO_2 catalysts: IA/ceria (blue); MO/ceria (red); MU/ceria (green); NP/ceria (black).

Catalytic CO oxidation activities were evaluated, and the results are shown in Figure 6A. It can be observed that the activities rank as IA/ceria < MO/ceria < MU/ceria < NP/ceria. IA/ceria and MO/ceria are almost inactive below 300 °C. However, the CO conversion over MU/ceria and NP/ceria are close to 100% at 200 and 100 °C, respectively. Clearly, the morphology of the Au species plays a key role in CO oxidation, and up to two atomic layer of gold is necessary for low temperature CO oxidation activity in the Au/CeO_2 system.

To understand the morphological effects of gold cluster on CO oxidation, the kinetic performance of the Au/CeO_2 catalysts were evaluated. The results are shown in Figure 6B and summarized in Table 1. It can be found that IA/ceria shows the highest apparent activation energies (E_a, ~83.9 kJ·mol^{-1}) of CO oxidation compared to other catalysts. Although the E_a of MO/ceria became lower than IA/ceria, it is still high (~72.8 kJ·mol^{-1}). However, the formation of multilayer Au species remarkably lowers the E_a to 57.3 kJ·mol^{-1}, and it is only 49.1 kJ/mol in the case of NP/ceria. Obviously, the activation energies of CO oxidation over Au/CeO_2 catalysts decrease linearly as the reducibility of the interfacial —Au—O—Ce— species increases.

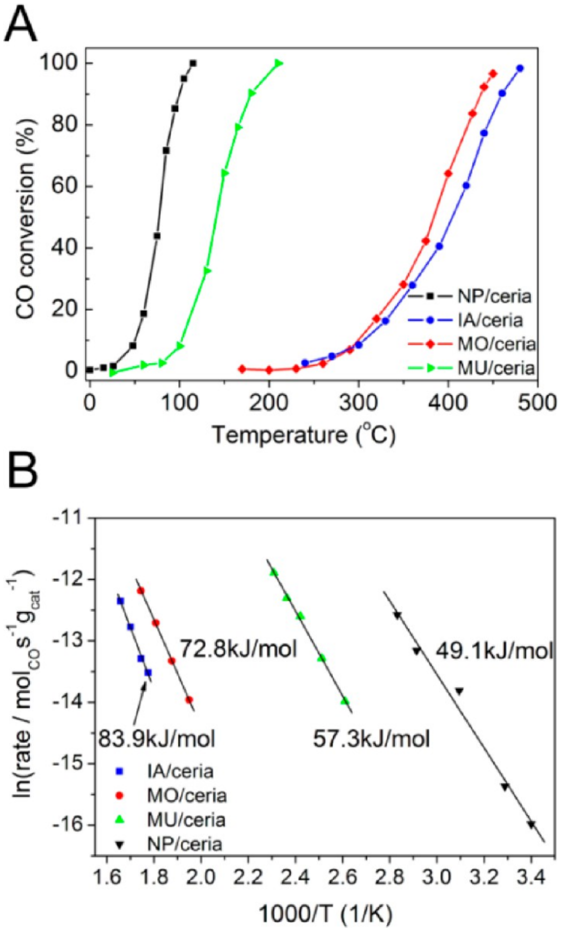

Figure 6. (A) CO conversion as a function of temperature; (B) Arrhenius plots of CO reaction rates of Au/CeO_2 catalysts: IA/ceria (blue); MO/ceria (red); MU/ceria (green); NP/ceria (black).

Table 1. Gold Loading, TOF Values (at 513 K) Based on All Au Atoms and the Apparent Activation Energies (E_a) of the CO Oxidation

samples	Au loading/wt %	TOF/s^{-1}	E_a/kJ·mol^{-1}
IA/ceria	0.42	1.07×10^{-2}	83.93
MO/ceria	1.66	2.42×10^{-3}	72.75
MU/ceria	1.66	4.89×10^{-2}	57.25
NP/ceria	1.67	9.88×10^{-1}	49.11

TOF values were also calculated, with the assumption that all gold atoms in the catalysts were accessible. As expected, NP/ceria is the most active catalyst, followed by MU/ceria, the activity of which is superior to MO/ceria and IA/ceria. At 513 K, the TOF values of NP/ceria and MU/ceria are 9.88×10^{-1} and 4.89×10^{-2} s^{-1}, respectively. With respect to MO/ceria and IA/ceria, however, it is very strange that the more reducible MO/ceria, with lower activation energies of CO oxidation, shows a lower TOF value (2.42×10^{-3} s^{-1}) than that of IA/ceria (1.07×10^{-2} s^{-1}). The abnormal results are likely attributed to the TOF calculation method, which ignore the inaccessibility of oxygen atoms of —Au—O—Ce— species at the metal—support interface. In fact, the contact structure of gold-support is of great importance because only the interface perimeter around the Au particles act as the reaction

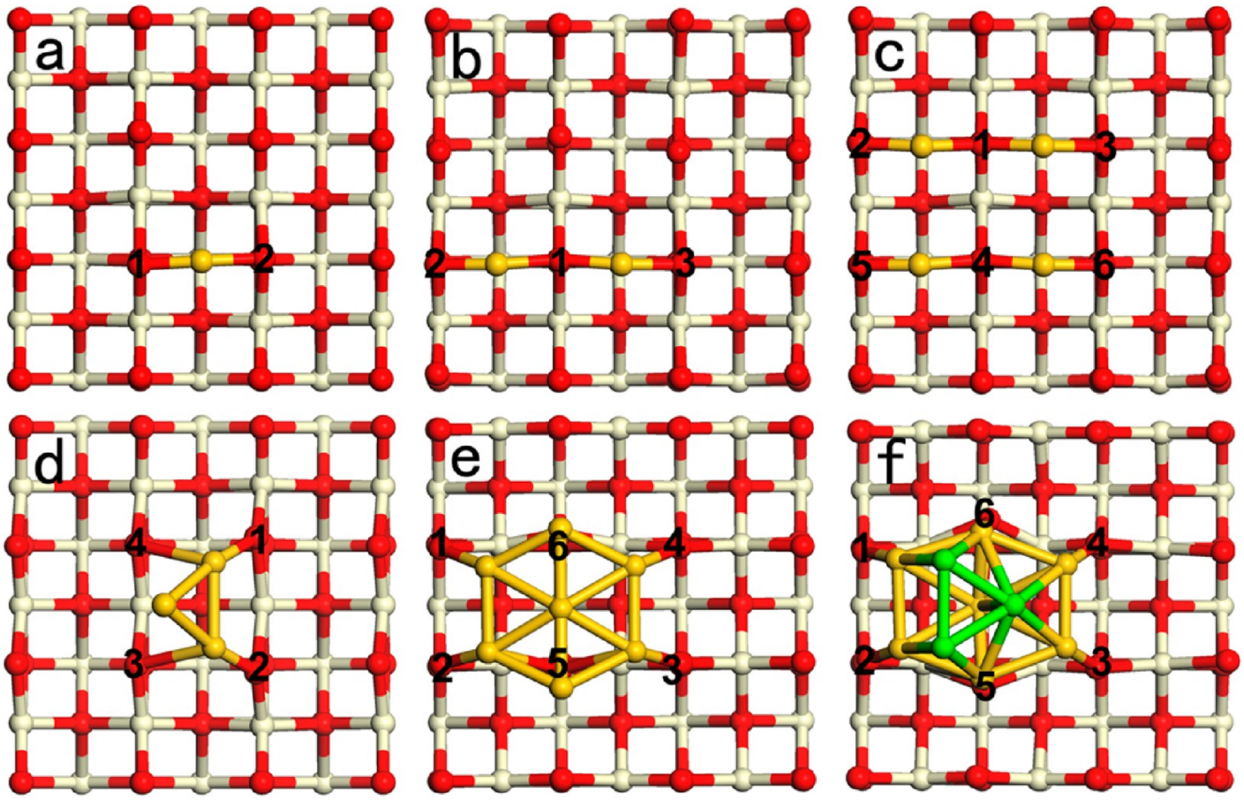

Figure 7. Most stable adsorption structures of $Au_n@CeO_2$ (100) (n = 1, 2, 3, 4, 7, 10), Au, O and Ce atoms are in gold, red and white, respectively. The top-layer of Au10 cluster marked with green color in f.

site.[16,17,22,51] For the IA/ceria catalyst, all the gold and the oxygen atoms of the −Au−O−Ce− species are accessible, whereas in the case of MO/ceria, except for those at the perimeter of gold monolayers, most of the oxygen atoms of −Au−O−Ce− species are inaccessible due to steric hindrance. These results reaffirm the idea that the interface perimeters are the active sites for CO oxidation. That is, the adsorbed CO molecules were oxidized by reactive oxygen species supplied by gold−ceria interface perimeters with formation of oxygen vacancy, and then O_2 was restored and incorporated into the lattice to complete the redox cycle.[52]

To gain insight into the strong morphology-dependent reducibility of the interfacial −Au−O−Ce− species, DFT calculations were carried out. Various possible adsorption sites were evaluated for Au single atoms and larger clusters to find the most stable and rational geometries, which is shown in Figure S18−S20. Due to the current practical limit of DFT calculations for large NPs, we focused on six Au clusters (Au_1, Au_2, Au_3, Au_4, Au_7, and Au_{10}) with three types of morphologies (i.e., individual atom, monolayer, and bilayer). Figure 7 shows the most stable and rational geometries of $Au_n@CeO_2$ (100). Because the performance of ceria-based materials is sensitive to the formation of oxygen vacancy (V_O), the oxygen vacancy formation energies (E_{vac}) of all oxygen in the perimeter of interface were calculated (Figure 8) because these oxygen atoms are considered active for CO oxidation.[53]

$Au_1@CeO_2$ and $Au_2@CeO_2$ have been chosen as representatives for the IA/ceria sample, and $Au_3@CeO_2$ and $Au_7@CeO_2$ for MO/ceria. When Au adatoms are located on Ce-top site and just coordinated with two oxygen atoms, the resulting geometry is the most stable structure (Figure 7a). The minimum E_{vac} of single atom configurations are found to be 2.69 and 1.56 eV for $Au_1@CeO_2$ and $Au_2@CeO_2$, respectively. Once Au was deposited on the ceria surface, new Au−O bonds could be formed. Due to the formation of Au−O bonds, the removal of the interfacial O is even more difficult than for other surface oxygen atoms that are located away from the interfaces (denoted as O_0, with E_{vac} being 1.36 eV).

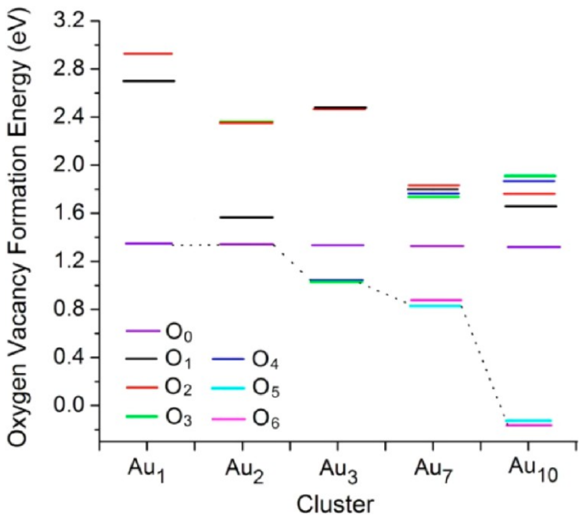

Figure 8. Oxygen vacancy formation energies (E_{vac}) of $Au_n@CeO_2(100)$, O_x denotes the oxygen vacancy of O atom numbered x, O_0 is surface oxygen away from interface.

In the case of the Au monolayer structure, the Au_3 cluster has a triangular configuration, and the Au_3 triangular plane titled toward the surface with two Au atoms making contact with two surface oxygen atoms[54] (Figure 7d), which is similar to Au_3 on

CeO_2 (111).[47] The Au_7 cluster was arranged in a hexagonal structure, which lies almost parallel to the ceria surface, and the six surrounding atoms bind to six surface oxygen atoms of ceria (Figure 7e). Top views of both structures show that each Au atom mostly occupies the top position of the Ce atom, which agrees well with the structure of MO/ceria. The E_{vac} of Au_3@CeO_2 and Au_7@CeO_2 are 1.02 and 0.82 eV, respectively. Although the E_{vac} is lower than that of the single atom configurations, the oxygen vacancy formation process is still endothermic and thermodynamically unfavorable. With Au_7 cluster as a starting configuration, we arranged three Au atoms above the Au_7 cluster, forming a model of bilayer structure (Au_{10}@CeO2), to better investigate the role of multilayer Au morphology in the reducibility of Au/CeO_2. As shown in Figure 7f, the Au cluster has two atomic layers, with 7 atoms in the hexagonal shaped bottom layer and 3 atoms in the top layer. In the case of the bilayer structure (Au_{10}@CeO_2), the minimum E_{vac} of interfacial oxygen become −0.16 eV, which is consisted with our previously studies.[19] The negative value suggests that surface oxygen is activated by the Au_{10} cluster, the removal of which is an exothermic process. Obviously, the E_{vac} decreases with transformation of the morphologies of Au clusters from single atom to monolayer and bilayer, and the E_{vac} changes from positive to negative when the bilayer structure appears. The bilayer structure is a necessary morphology of Au species to improve reducibility and activity of surface oxygen in the Au/CeO_2 system. These DFT calculations are in accord with the experimental results, and both demonstrate the importance of morphologies of gold clusters for activity of surface oxygen.

It is well-known that surface V_O would supply very stable anchoring sites for Au clusters. To rule out the effect of stronger adsorption energies of gold atoms on oxygen vacancy sites, the configuration for one gold atom adsorbed on the oxygen vacancy site was constructed (Figure S21), and the E_{ad} reached up to 5.20 eV. However, the E_{ad} of a single gold atom supported on the surface after interfacial oxygen extraction is 2.17 eV, which is even lower than the adsorption energy of the stoichiometric CeO_2 surface (3.50 eV). In addition, the positions of individual gold atoms remain almost unchanged after interfacial oxygen extraction (Figure S22). Furthermore, the energy of the Au cluster binding to the oxygen vacancy varies with the Au cluster size. The difference of adsorption energy of a single Au atom supported on between stoichiometric surface and a reduced surface of ceria is very apparent, differing by 1.25 eV in energy.[55] With the increase of Au cluster size, the difference of adsorption energy becomes smaller (∼0.2 eV) for the Au_{13} cluster supported on ceria.[53] Therefore, as the cluster size increases, the energy difference resulting from the strong adsorption energy of gold clusters on oxygen vacancy sites is negligible. Because of the interaction between Au−Au in larger clusters, adsorption structures of Au_n@CeO_2 after interfacial oxygen extraction underwent smaller changes.

To understand the origin of E_{vac} lowering, two aspects, charge transfer and local reconstruction, should be considered. The profiles of atomic Bader charge analysis were summarized in Table S3. It is found that some electrons are transferred from Au clusters to the ceria surface upon adsorption, leading to the formation of a slightly positive charged Au.[21,56] The excess charge in the substrate is mostly localized around Ce atoms of −Au−O−Ce species (Figure S23), yielding the partially reduced Ce ion.[55] The O atoms attached directly to Au atoms became slightly less negative. This process weakens the Ce−O bond and activates surface oxygen effectively. In addition, the reconstruction of the local structure is also beneficial for activation of the interfacial oxygen. For instance because of the combined effect of two Au atoms, the O_1 atom in Au_2@CeO_2 moves away from the surface approximately 0.34 Å, resulting in the drop of E_{vac} compared with Au_1@CeO_2, and a 0.42 Å deviation is observed for O_6in the Au_7@CeO_2 configuration, as well as a significant structural rearrangement of Au_7 cluster upon adsorption (Figure S24), folding the cluster into a 138.8 degree angle between two planes, indicating that the MO structure is unstable against local reconstruction. This structural transformation is a manifestation of the “structural fluxionality” of clusters.[57,58] In the case of the bilayer gold clusters, Au_{10}, it is constructed by a first-layer Au_7 and top-layer triangular Au_3[59] (marked with green color in Figure 7). Because of the strong Au−Au bond between the two layers,[47,60] Au_{10} is stable against structural fluxionality.[61] Once Au_{10} is deposited on the ceria surface, the O_6 in Au_{10}@CeO_2 deviates significantly (∼0.8 Å) from the initial site to minimize the energy of the system. Therefore, due to the combination effects of electron transfer and local reconstruction, the interfacial oxygen of Au_{10}@CeO_2 is more active than in other configurations.

4. CONCLUSIONS

We prepared a series of Au/CeO_2 catalysts (IA/ceria, MO/ceria, MU/ceria and NP/ceria) with different gold morphologies using well-defined {100}-faceted ceria NCs as supports. Strong dependence on gold morphology for reducibility and catalytic CO oxidation activity was identified. It was shown that gold clusters with up to two atomic layers were necessary for good reducibility and CO oxidation activity in Au/CeO_2 catalysts. These findings will be beneficial for further exploration of the origin of high activity of gold catalysts, as well as for the design and synthesis of advanced catalysts.

■ ASSOCIATED CONTENT

Ⓢ Supporting Information

The following file is available free of charge on the ACS Publications website at DOI: 10.1021/cs502055r.

> TEM and HRTEM images, XRD and XPS results of catalysts; quantitative analysis of HAADF-STEM images and theoretical calculations results (PDF)

■ AUTHOR INFORMATION

Corresponding Author

*E-mail: kbzhou@ucas.ac.cn.

Notes

The authors declare no competing financial interest.

■ ACKNOWLEDGMENTS

This work was supported by the National Natural Science Foundation of China (21473199 and 91127018) and Beijing Municipal Science & Technology Commission.

■ REFERENCES

(1) Haruta, M.; Tsubota, S.; Kobayashi, T.; Kageyama, H.; Genet, M. J.; Delmon, B. *J. Catal.* **1993**, *144*, 175−192.

(2) Zhu, Y.; Qian, H. F.; Drake, B. A.; Jin, R. *Angew. Chem., Int. Ed.* **2010**, *49*, 1295−1298.

(3) Hashmi, A. S. K.; Hutchings, G. J. *Angew. Chem., Int. Ed.* **2006**, *45*, 7896−7936.

(4) Takei, T.; Akita, T.; Nakamura, I.; Fujitani, T.; Okazaki, M. O. K.; Huang, J.; Ishida, T.; Haruta, M. In *Advances in Catalysis*; Gates, B. C., Jentoft, F. C., Eds.; Elsevier: Amsterdam, 2012; Vol. *55*, pp 1−126
(5) Haruta, M.; Yamada, N.; Kobayashi, T.; Iijima, S. *J. Catal.* **1989**, *115*, 301−309.
(6) Yoon, B.; Hakkinen, H.; Landman, U.; Worz, A. S.; Antonietti, J.-M.; Abbet, S. p.; Judai, K.; Heiz, U. *Science* **2005**, *307*, 403−407.
(7) Valden, M.; Lai, X.; Goodman, D. W. *Science* **1998**, *281*, 1647−1650.
(8) Chen, M. S.; Goodman, D. W. *Science* **2004**, *306*, 252−255.
(9) Herzing, A. A.; Kiely, C. J.; Carley, A. F.; Landon, P.; Hutchings, G. J. *Science* **2008**, *321*, 1331−1335.
(10) Song, W.; Hensen, E. J. M. *ACS Catal.* **2014**, *4*, 1885−1892.
(11) Li, L.; Gao, Y.; Li, H.; Zhao, Y.; Pei, Y.; Chen, Z. F.; Zeng, X. C. *J. Am. Chem. Soc.* **2013**, *135*, 19336−19346.
(12) Huang, W.; Bulusu, S.; Pal, R.; Zeng, X. C.; Wang, L.-S. *ACS Nano* **2009**, *3*, 1225−1230.
(13) Jia, C.-J.; Liu, Y.; Bongard, H.; Schuth, F. *J. Am. Chem. Soc.* **2010**, *132*, 1520−1522.
(14) Green, I. X.; Tang, W.; Neurock, M.; Y, J. T., Jr. *Science* **2011**, *333*, 736−739.
(15) Trovarelli, A. *Catal. Rev.: Sci. Eng.* **1996**, *38*, 439−520.
(16) Fu, Q.; Saltsburg, H.; Flytzani-Stephanopoulos, M. *Science* **2003**, *301*, 935−938.
(17) Yi, N.; Si, R.; Saltsburg, H.; Flytzani-Stephanopoulos, M. *Energy Environ. Sci.* **2010**, *3*, 831−837.
(18) Si, R.; Flytzani-Stephanopoulos, M. *Angew. Chem., Int. Ed.* **2008**, *47*, 2884−2887.
(19) Wang, L.; Lu, G.; Yang, D.; Wang, J.; Zhu, Z. B.; Wang, Z. X.; Zhou, K. B. *Chem. Catal. Chem.* **2013**, *5*, 1308−1312.
(20) Guzman, J.; Carrettin, S.; Corma, A. *J. Am. Chem. Soc.* **2005**, *127*, 3286−3287.
(21) Song, W.; Hensen, E. J. M. *J. Phys. Chem. C* **2013**, *117*, 7721−7726.
(22) Carrettin, S.; Concepcion, P.; Corma, A.; Lopez Nieto, J. M.; Puntes, V. F. *Angew. Chem., Int. Ed.* **2004**, *43*, 2538−2540.
(23) Zhou, K.; Li, Y. *Angew. Chem., Int. Ed.* **2012**, *51*, 602−613.
(24) Wu, Z.; Li, M.; Mullins, D. R.; Overbury, S. H. *ACS Catal.* **2012**, *2*, 2224−2234.
(25) Sa, J.; Goguet, A.; Taylor, S. F. R.; Tiruvalam, R.; Kiely, C. J.; Nachtegaal, M.; Hutchings, G. J.; Hardacre, C. *Angew. Chem., Int. Ed.* **2011**, *50*, 8912−8916.
(26) Nolan, M. *Chem. Phys. Lett.* **2010**, *499*, 126−130.
(27) Goguet, A.; Hardacre, C.; Harvey, I.; Narasimharao, K.; Saih, Y.; Sa, J. *J. Am. Chem. Soc.* **2009**, *131*, 6973−6975.
(28) Sá, J.; Taylor, S. F. R.; Daly, H.; Goguet, A.; Tiruvalam, R.; He, Q.; Kiely, C. J.; Hutchings, G. J.; Hardacre, C. *ACS Catal.* **2012**, *2*, 552−560.
(29) De Backer, A.; Martinez, G. T.; Rosenauer, A.; Van Aert, S. *Ultramicroscopy* **2013**, *134*, 23−33.
(30) Van Aert, S.; Verbeeck, J.; Erni, R.; Bals, S.; Luysberg, M.; Van Dyck, D.; Van Tendeloo, G. *Ultramicroscopy* **2009**, *109*, 1236−1244.
(31) Van Aert, S.; Batenburg, K. J.; Rossell, M. D.; Erni, R.; Van Tendeloo, G. *Nature* **2011**, *470*, 374−377.
(32) Li, Z. Y.; Young, N. P.; Di Vece, M.; Palomba, S.; Palmer, R. E.; Bleloch, A. L.; Curley, B. C.; Johnston, R. L.; Jiang, J.; Yuan, J. *Nature* **2008**, *451*, 46−48.
(33) Peterson, E. J.; DeLaRiva, A. T.; Lin, S.; Johnson, R. S.; Guo, H.; Miller, J. T.; Kwak, J. H.; Peden, C. H. F.; Kiefer, B.; Allard, L. F.; Ribeiro, F. H.; Datye, A. K. *Nat. Commun.* **2014**, *5*, 4885.
(34) Uzun, A.; Ortalan, V.; Hao, Y.; Browning, N. D.; Gates, B. C. *J. Phys. Chem. C* **2009**, *113*, 16847−16849.
(35) Qiao, B.; AiqinWang; Yang, X.; Allard, L. F.; Jiang, Z.; Cui, Y.; Liu, J.; Li, J.; Zhang, T. *Nat. Chem.* **2011**, *3*, 634−641.
(36) Corma, A.; Mercedes, Boronat1; Sabater, Maria J.; Navas, Javier; Yacaman, Miguel José; Larios, Eduardo; Posadas, Alvaro; López-Quintela, M. Arturo; Buceta, David; Ernest, Mendoza; G, G.; M, A. *Nat. Chem.* **2013**, *5*, 775−781.
(37) Epicier, T.; Sato, K.; Tournus, F.; Konno, T. *J. Nanopart. Res.* **2012**, *14*, 1106.
(38) Bals, S.; Van Aert, S.; Romero, C. P.; Lauwaet, K.; Van Bael, M. J.; Schoeters, B.; Partoens, B.; Yucelen, E.; Lievens, P.; Van Tendeloo, G. *Nat. Commun.* **2012**, *3*, Articleno. 897−6.
(39) Liu, Y.; Jia, C.-J.; Yamasaki, J.; Terasaki, O.; Schuth, F. *Angew. Chem., Int. Ed.* **2010**, *49*, 5771−5775.
(40) Lengke, M. F.; Ravel, B.; Fleet, M. E.; Wanger, G.; Gordon, R. A.; Southam, G. *Environ. Sci. Technol.* **2006**, *40*, 6304−6309.
(41) Costello, C. K.; Guzman, J.; Yang, J. H.; Wang, Y. M.; Kung, M. C.; Gates, B. C.; Kung, H. H. *J. Phys. Chem. B* **2004**, *108*, 12529−12536.
(42) Calla, J. T.; Davis, R. J. *Catal. Lett.* **2005**, *99*, 21−26.
(43) Guzman, J.; Kuba, S.; Fierro-Gonzalez, J. C.; Gates, B. C. *Catal. Lett.* **2004**, *95*, 77−86.
(44) Guzman, J.; Gates, B. C. *Nano Lett.* **2001**, *1*, 689−692.
(45) Deng, W.; Frenkel, A. I.; Si, R.; Flytzani-Stephanopoulos, M. *J. Phys. Chem. C* **2008**, *112*, 12834−12840.
(46) Miller, J. T.; Kropf, A. J.; Zha, Y.; Regalbuto, J. R.; Delannoy, L.; Louis, C.; Bus, E.; van Bokhoven, J. A. *J. Catal.* **2006**, *240*, 222−234.
(47) Zhang, C.; Michaelides, A.; King, D. A.; Jenkins, S. J. *J. Am. Chem. Soc.* **2010**, *132*, 2175−2182.
(48) Hutchings, G.; Hall, M.; Carley, A.; Landon, P.; Solsona, B.; Kiely, C.; Herzing, A.; Makkee, M.; Moulijn, J.; Overweg, A. *J. Catal.* **2006**, *242*, 71−81.
(49) Karpenko, A.; Leppelt, R.; Plzak, V.; Behm, R. J. *J. Catal.* **2007**, *252*, 231−242.
(50) Acerbi, N.; Tsang, S. C.; Golunskib, S.; Collier, P. *Chem. Commun.* **2008**, 1578−1580.
(51) Haruta, M. *CATTECH* **2002**, *6*, 102−115.
(52) Ta, N.; Liu, J.; Chenna, S.; Crozier, P. A.; Li, Y.; Chen, A.; Shen, W. *J. Am. Chem. Soc.* **2012**, *134*, 20585−20588.
(53) Kim, H. Y.; Lee, H. M.; Henkelman, G. *J. Am. Chem. Soc.* **2012**, *134*, 1560−1570.
(54) Zhu, W.-J.; Zhang, J.; Gong, X.-Q.; Lu, G. *Catal. Today* **2011**, *165*, 19−24.
(55) Camellone, M. F.; Fabris, S. *J. Am. Chem. Soc.* **2009**, *131*, 10473−10483.
(56) Teng, B.-T.; Lang, J.-J.; Wen, X.-D.; Zhang, C.; Fan, M.; Harris, H. G. *J. Phys. Chem. C* **2013**, *117*, 18986−18993.
(57) Hakkinen, H.; Abbet, S.; Sanchez, A.; Heiz, U.; Landman, U. *Angew. Chem., Int. Ed.* **2003**, *42*, 1297−1300.
(58) Rashkeev, S.; Lupini, A.; Overbury, S.; Pennycook, S.; Pantelides, S. *Phys. Rev. B* **2007**, *76*, 035438.
(59) Teng, B. T.; Wu, F. M.; Huang, W. X.; Wen, X. D.; Zhao, L. H.; Luo, M. F. *ChemPhysChem* **2012**, *13*, 1261−1271.
(60) Çakır, D.; Gülseren, O. *J. Phys. Chem. C* **2012**, *116*, 5735−5746.
(61) Han, Z. K.; Gao, Y. *Nanoscale* **2015**, *7*, 308−316.